Giner-Sanz, JJ.; Ortega Navarro, EM.; Pérez-Herranz, V. (2018). Mechanistic equivalent circuit modelling of a commercial polymer electrolyte membrane fuel cell. Journal of Power Sources. 379:328-337. https://doi.org/10.1016/j.jpowsour.2018.01.066

Mechanistic equivalent circuit modelling of a commercial Polymer Electrolyte Membrane fuel cell

J. J. Giner-Sanz, E. M. Ortega, V. Pérez-Herranz*

IEC group, Depto. Ingeniería Química y Nuclear, Universitat Politècnica de València

Camino de Vera S/N, 46022 Valencia, Spain

*Corresponding author. Tel.: +34-96-3877632; fax: +34-96-3877639;

E-mail address: vperez@iqn.upv.es (V. Pérez-Herranz)

Abstract

Electrochemical impedance spectroscopy (EIS) has been widely used in the fuel cell field since it allows deconvolving the different physic-chemical processes that affect the fuel cell performance. Typically, EIS spectra are modelled using electric equivalent circuits. In this work, EIS spectra of an individual cell of a commercial PEM fuel cell stack were obtained experimentally. The goal was to obtain a mechanistic electric equivalent circuit in order to model the experimental EIS spectra. A mechanistic electric equivalent circuit is a semiempirical modelling technique which is based on obtaining an equivalent circuit that does not only correctly fit the experimental spectra, but which elements have a mechanistic physical meaning. In order to obtain the aforementioned electric equivalent circuit, 12 different models with defined physical meanings were proposed. These equivalent circuits were fitted to the obtained EIS spectra. A 2 step selection process was performed. In the first step, a group of 4 circuits were preselected out of the initial list of 12, based on general fitting indicators as the determination coefficient and the fitted parameter uncertainty. In the second step, one of the 4 preselected circuits was

selected on account of the consistency of the fitted parameter values with the physical meaning of each parameter.

Keywords: Electrochemical Impedance Spectroscopy (EIS), PEM fuel cell, Mechanistic electric equivalent circuit, Low frequency inductive loop, Semiempirical modelling.

1. Introduction

Fuel Cells (FCs) are electrochemical devices that are able to directly transform the chemical energy of the fuel oxidation reaction into electricity [1]. In the last decades, Proton Exchange Membrane FC (PEMFC) have raised as promising alternatives for power generation devices for automotive, portable and distributed applications [2], on account of their high power density, compactness and light weight [3, 4]. In recent years, a great amount of research has been focused on increasing the performance [5] and the durability of PEMFC [6], and on decreasing their cost [7]. Numerous studies have focused on the different elements of a FC: membranes [8, 9], gas diffusion layers [10-14], catalyst layers [15-18], and flow fields [19].

The main characteristic of a FC is its polarization curve, which corresponds with the steady state measurement of the cell voltage versus the delivered current intensity [20]. However, this steady state measurement does not allow the distinction of single processes. If single loss factors have to be distinguished, dynamic measurements are needed [21]. Nowadays, Electrochemical Impedance Spectroscopy (EIS) has gained significant relevance in the FC field, since this dynamic electrochemical measurement technique allows to obtain information on the fuel cell internal state and on its electrochemical behavior [22, 23]. This technique provides meaningful information for both, the development and the operation of FCs. On the one hand, from the operator's point of view, EIS allows to determine the humidification level of the membrane and if the gas diffusion layers are flooded. On the other hand, from the developer's point of view, EIS is useful in order to quantify the charge transfer, the contact, and the mass

transport resistances; assessing in this manner, any of the designed elements [24]. The wide range of applications of EIS within the FC field is due to the fact that this electrochemical method is able to deconvolve the different physic-chemical phenomena that take place in the system at different timescales [25]; allowing to obtain a large number of electrochemical properties of the system such as electrolyte properties (i.e. ohmic resistance and proton conductivity), electrode properties (i.e. double layer capacitance and charge transfer resistance), and mass transport properties (i.e. diffusion coefficients and effective concentrations) [26].

EIS is a frequency domain method that consists in the application of a monofrequency sinusoidal perturbation signal (voltage or current) to a given system; and the measurement of the generated output signal (current or voltage) [27, 28]. From the ratio of the amplitudes of both signals, and from the phase difference between them, the complex impedance of the system at the excited frequency is determined [29]. A frequency sweep is performed: the process is repeated for different perturbation frequencies [30]. With this procedure, the EIS spectrum of the system, consisting in the complex impedance of the system at the different excited frequencies, is obtained [31].

One possible way to interpret an EIS spectrum is in terms of models. There are two types of models for interpreting EIS data [32]: analogs and physical models. On the one hand, analogs, generally in the form of electrical equivalent circuits (EEC), follow an empirical modelling methodology: they just seek to reproduce the experimental behaviour of the impedance, without considering the physico-electrochemical properties of the system. This modelling strategy has been used in a great number of works in literature [33-45].

The great advantage of this type of models is that they do not require nearly any knowledge of the system: an EEC can be proposed just by pattern recognition, without identifying any of the real processes that take place in the system [29]. In return, this type of model does not provide any insight of the mechanisms of the phenomena that take place.

On the other hand, physical models try to reproduce the impedance behaviour of the system by taking into account the physical mechanism of the different electrochemical processes. De Levie was the pioneer of this approach [46]: he determined the analytical solution for the impedance model of a porous electrode subject to a potential gradient, considering linear kinetics and no concentration differences [47]. Lasia extended this model in order to consider Buttler-Volmer kinetics [48], and to consider concentration gradients [49]. The aforementioned porous electrode model with concentration gradient is the foundation of now-a-days impedance models [46]. Springer and co-workers developed one of the first PEMFC impedance models [50], which consisted in a 1D macro-homogeneous model of the gas diffusion layer and the catalyst layer of a PEMFC. Guo and White extended Springer's model, considering a flooded agglomerate model for the catalyst layer [51]. Kulikovski developed an analytical impedance model for catalyst layers of PEMFCs [52-55]. All the works mentioned above focus mainly on charge and mass transport. Other works have focused on the low-frequency behavior of PEMFCs (i.e. low-frequency inductive semicircle). Some of them have attributed the low-frequency features to water transport phenomena [56-60]; others have attributed them to ORR intermediated buildup [61-63]; and finally, others have attributed them to PtO formation [62, 64]. Extensive reviews on the state-of-the-art PEMFC impedance

modelling can be found in literature [36, 65-66]. The advantage of this type of models is that it allows unveiling and studying the different electrochemical processes taking place in the system. However, real physical models can be hard to obtain, especially for complex electrochemical processes [30].

In this work, a semiempirical modelling methodology was selected. This hybrid between the analog and the physical model combines the advantages of both methodologies. The semiempirical model considered in this case was a mechanistic EEC: an EEC which elements have clearly defined mechanistic physical meanings. This work's aim is to obtain a mechanistic EEC for an individual cell of a commercial PEMFC stack. In order to fulfil this goal, the experimental EIS spectrum of the considered system was measured. Then, different mechanistic EECs were proposed and fitted to the experimental spectrum. The EEC that resulted in a better fitting and whose fitted parameters had physically consistent values was selected.

2. Experimental work

Figure 1 shows the experimental setup used in this work. Its main element is a 300W commercial PEMFC stack, provided by HeliocentriS®, composed by 20 individual cells, with an effective area of 58 cm^2. The air supply is provided by a compressor and the hydrogen comes from a 200 bar high-pressure storage tank. The humidification of the gas inlets is assured by a humidification system and the fuel cell stack operating temperature is controlled by a refrigeration system. The humidification system consists in two independent bubbling humidification systems, with humidification temperature control. And the refrigeration system consists in a heat exchanger equipped with a continuous pump and a temperature controller. The reactant gases flow rates are controlled using mass flow controllers. The reactant inlet pressures are monitored by pressure gauges and are regulated using manual valves. All the relevant system temperatures are monitored by thermocouples. The overall control was done using a control computer with a Labview® application. All the experiments were carried out in open end anode mode, with constant inlet reactant flow rates: $5\ NL \cdot min^{-1}$ for the hydrogen stream and $35\ NL \cdot min^{-1}$ for the air stream. All the experiments were performed in the same operation conditions: an operation temperature of $30℃$; and the same humidification temperature for both gases, $30℃$.

The individual cell galvanostatic impedance spectra were obtained using an Autolab® 302N potentiostat/galvanostat with FRA module and 20A booster, controlled using NOVA® software. The selected frequency range extended from 5 kHz to 10 mHz, with 50 frequencies logarithmically spaced. The spectra were measured for 3 different

polarization currents: 1A ($\approx 17\ mA \cdot cm^{-2}$), 4A ($\approx 69\ mA \cdot cm^{-2}$) and 8A ($\approx 138\ mA \cdot cm^{-2}$); and with the optimum perturbation amplitude determined in a previous work [67]. Table 1 lists the measurement parameters used to perform the EIS measurements in this work; they correspond with the optimum measurement parameters obtained in a previous work [68].

The I-V polarization curve was obtained by galvanodynamic sweep. The intensity sweep was done in increasing sense, starting at 0.0 A; with a sweep speed of $3.0\ mA \cdot s^{-1}$, since it was observed in preliminary studies that this sweep speed was slow enough to reach the quasi steady state for each applied current. The DC resistance for each considered operation current was obtained from the slope of the polarization curve at the corresponding operation point [69].

The I-V polarization curve and the EIS spectra at the 3 considered operation currents were obtained in triplicate in order to control the reproducibility of the obtained results. Replicates of each measurement were not performed sequentially; instead, the order of the experiments was randomized. The randomization strategy allows to orthogonalize the studied factors and the time factor: therefore, it allows identifying any possible time drifts.

A 15 min preconditioning was performed before each measurement in order to assure that the state of the system was the same in all the experiments. The preconditioning was done at the DC current associated to the experiment that was going to be performed; and at 1.0 A, in the case of the polarization curves.

3. Results and discussion

3.1. Experimental EIS spectra

Figure 2 shows the experimental EIS spectra of the studied single PEMFC cell. It can be observed that the spectra are composed by an inductive feature at high frequencies, one or two depressed capacitive loops, and an inductive loop at low frequencies.

First, it is well known that high frequency inductive features are generally generated by the cables of the measurement system [70]. Second, one of the capacitive loops shrinks when the operation current is increased; whereas, the other capacitive loop expands with an increase of the operation current. It can be deduced that the first capacitive loop is related to charge transfer [71], while the second one is related to mass transfer [72]. Moreover, the high frequency capacitive loop prescribes a straight line at high frequencies that forms an angle with the real axis slightly higher than $45°$. It has been proved that this characteristic of the spectra is due to distributed resistance in the cathodic catalyst layer [73-74]. Third, many explanations have been proposed in literature for low frequency inductive loops: adsorption and desorption in heterogeneous reactions, adsorbed reaction intermediates, Pt dissolution, and water transport in the membrane, amongst others [75]. Since the inductive loop shrinks with an increase in the polarization current, the most probable cause of the observed inductive loop is the adsorption and desorption of reaction intermediates [76]. Finally, the high frequency intercept of the spectra with the real axis does not correspond with

the origin of the complex plane: this intercept gives the internal ohmic resistance of the fuel cell [29].

3.2. Electric equivalent circuit candidates

3.2.1. Nomenclature and definitions

Figure 3 shows the symbols used in this work for each one on the elements of electric equivalent circuits. On the one hand, in this work, the following definition was considered for the constant phase element [77]:

$$Z_{CPE} = \frac{1}{Q_{CPE} \cdot (j \cdot \omega)^{\alpha_{CPE}}} \quad (1)$$

On the other hand, the definition considered in this work for a generalized finite length Warburg element was [77]:

$$Z_W = \frac{R_{tm}}{(j \cdot \omega \cdot \tau_{tm})^{\alpha_{tm}}} \cdot tanh[(j \cdot \omega \cdot \tau_{tm})^{\alpha_{tm}}] \quad (2)$$

3.2..2. General assumptions

The impedance of an individual PEMFC can be broken down into 4 separate contributions [78]:

$$Z = Z_{cables} + Z_{anode} + Z_{PEM} + Z_{cathode} \quad (3)$$

On the one hand, $Z_{cathode}$ denotes the cathodic impedance. It includes the impedance contribution of the cathodic bipolar plate (BP), the cathodic gas diffusion layer (GDL) and the cathodic catalyst layer (CL). Analogously, Z_{anode} denotes the anodic impedance. It encompasses the impedance of the anodic BP, the anodic GDL and the anodic CL. On the other hand, Z_{PEM} represents the impedance of the PEM membrane. Finally, Z_{cables} denotes the impedance of the measurement instrument cabling. It should be noted that strictly speaking Z_{cables} is not part of the PEMFC itself. However, it is generally considered since experimental EIS spectra include the contribution of the instrumental cabling [29].

In most cases, the resistance of the cabling is negligible; whereas its reactance is not [31]. The most common approach is to consider that the measurement cables behave as pure inductors:

$$Z_{cables} = L_{cables} \quad (4)$$

A common approach is to group all the ohmic resistances within the PEMFC in a single resistance: the internal resistance of the cell, R_{int}. This resistance can be disaggregated into an electronic resistance, $R_{electronic}$; and into an ionic resistance, R_{ionic}:

$$R_{int} = R_{electronic} + R_{ionic} \quad (5)$$

On the one hand, the electronic resistance comprises all the resistance to electron flow in the electronic conductors of the PEMFC (i.e. Bipolar plates). On the other hand, the ionic resistance includes the resistance to the proton flow in the ionic conductors of the PEMFC (i.e. PEM membrane).

The usual approach for simulating impedance responses is to consider separately the faradic currents and the non-faradic currents [79]. This approach was questioned by Nisancioglu and Newman [80], since part of the flux of reacting species also contributes to the charging of the double-layer. This results in a coupling between the faradic and the non-faradic currents. However, Wu and co-workers showed that this coupling had a significant effect only at very high frequencies [81]. Since the considered frequency range does not include the high frequency range, in this work it was assumed that the faradic currents could be decoupled from the non-faradic ones.

In this work, 12 electric equivalent circuits with mechanistic explanation were considered. These 12 equivalent circuits were selected on the basis of the features identified on the experimental EIS spectra in section 3.1. In the following subsections, a brief description of each one of these equivalent circuits will be introduced.

3.2.3. Circuit 1

In circuit 1 both electrochemical reactions (Hydrogen Oxidation Reaction, HOR; and Oxygen Reduction Reaction, ORR) are assumed to significantly contribute to the PEMFC impedance. A typical RCPE subcircuit was considered to model the HOR; whereas, the

Harrington and Conway subcircuit for electrochemical reactions with adsorbed intermediates [82] was considered to model the ORR. Figure 4a shows circuit 1.

3.2.4. Circuit 2

Circuit 2, shown in figure 4b, is based on the same assumptions than circuit 1. In addition to these assumptions, circuit 2 considers mass transport limitations in the HOR. These mass transport limitations are modelled by including a finite length Warburg element in the subcircuit associated to HOR.

3.2.5. Circuit 3

Circuit 3, shown in figure 4c, assumes that HOR is significantly faster that ORR [83]. Under this assumption, the HOR impedance can be neglected with respect to the ORR impedance. Applying this assumption to circuit 1, the subcircuit related to HOR can be removed. In addition, in circuit 3, mass transport limitations in the ORR are considered. In this case, it was considered that the mass transport limitation affected both, the current associated with surface coverage changes (R_0 and L) and the current not associated with surface coverage changes (R_∞).

3.2.6. Circuit 4

Circuit 4 is based on the same assumptions than circuit 3, with the excpetion that it assumed that the mass transport limitation only affects the current not associated with surface coverage changes (R_∞). This circuit can be seen in figure 4d.

3.2.7. Circuit 5

Circuit 5, shown in figure 4e, assumes that the impedance related to HOR is negligible with respect to the impedance related to ORR, as in circuits 3 and 4. The only difference between circuit 5 and the other mentioned circuits, is that circuit 5 assumes that the mass transport limitation only affects the current associated with surface coverage changes (R_0 and L).

3.2.8. Circuit 6

Circuit 6 assumes that both reactions have significant contributions to the impedance of the PEMFC. In this case, a RCPE subcircuit is considered for both reactions. In addition, one of the reactions presents mass transport limitations. Finally, water transport phenomena are considered as well in circuit 6. In this circuit, the low frequency inductive loop is supposed to be due to the water transport phenomena [84]. This effect is modelled with an RL subcircuit in circuit 6, as shown in figure 4f.

3.2.9. Circuit 7

Circuit 7, shown in figure 4g, is based on circuit 2. In addition to the assumptions considered in the aforementioned circuit, in circuit 7 water transport phenomena are considered. In this case, these phenomena are modelled using an RCPE subcircuit [37].

3.2.10. Circuit 8

Circuit 8 is built from circuit 2. In addition, in circuit 8 the distributed resistance of the cathodic layer is considered [85]. In bibliography, the distributed resistance of the cathodic CL is generally modeled using a transmission line [74]. It can be shown that a transmission line is equivalent to a generalized finite length Warburg element [86]. For this reason, in circuit 8 the distributed resistance of the cathodic CL was modeled by a generalized finite length Warburg element, as it can be seen in figure 4h.

3.2.11. Circuit 9

Circuit 9, shown in figure 4i, is a variant of circuit 3 in which the distributed resistance of the cathodic CL is considered. The mentioned distributed resistance was modeled in circuit 9 using the same element than in circuit 8: a generalized finite length Warburg element.

3.2.12. Circuit 10

Circuit 10 is the modification of circuit 4 in order to include the distributed resistance of the cathodic CL, by adding a generalized finite length Warburg element. Circuit 10 is represented in figure 4j.

3.2.13. Circuit 11

Circuit 11 corresponds with the modified version of circuit 5 that takes into account the distributed resistance of the cathodic CL, by adding a generalized finite length Warburg element. Circuit 11 is given by figure 4k.

3.2.14. Circuit 12

Finally, circuit 12, shown in figure 4l, considers that the HOR is negligible in comparison with the ORR, modelled by a Harrington and Conway subcircuit. In addition, circuit 12 includes a generalized finite length Warburg element in order to model the distributed resistance of the cathodic CL. Moreover, circuit 12 also considers water transport phenomena. In this case, these phenomena are modeled by a generalized finite length Warburg element.

3.3. Circuit selection

3.3.1. Preliminary selection

Each of the 12 electric equivalent circuits listed in section 3.2 were fitted to the experimental EIS spectrum obtained at a polarization current of 8A, which was presented in section 3.1. In the preliminary selection step, only general fitting indicators were considered. On the one hand, figure 5a shows the determination coefficient (R^2) of the fitting of each one of the considered equivalent circuits to the experimental spectrum. On the other hand, figure 5b gives the total uncertainty in the fitted parameters, expressed as the mean error of the fitted parameters (s_{mean}), of each one of the considered equivalent circuits. This parameter is defined by:

$$s_{mean} = \frac{1}{N_{par}} \cdot \sum_{i=1}^{N_{par}} s_i = \frac{1}{N_{par}} \cdot \sum_{i=1}^{N_{par}} \frac{\sigma_i}{X_i} \cdot 100 \qquad (6)$$

Where N_{par} denotes the number of parameters in the considered equivalent circuit; and s_i is the relative error of the i-th fitted parameter, which is defined as the ratio (expressed in %) of the uncertainty associated with the i-th parameter (σ_i) and its fitted value (X_i).

Two criteria were used for the preliminary selection: maximization of the determination coefficient (i.e. better fitting) and minimization of the mean error of the fitted parameters (i.e. less uncertainty in the fitted parameters). As it can be observed in figures 5a and 5b, 4 circuits can be highlighted based on these criteria: circuits 9, 10, 11 and 12. For this reason, these were preselected in the preliminary selection step.

3.3.2. Selection refinement

In a second step, the selection was refined further using physical arguments. In this second selection step only the 4 preselected circuits were considered. The fitted parameters (and their errors) of each one of the 4 circuits are compiled in tables 2, 3, 4 and 5.

First, as it can be seen in table 4, the fitted value of parameter R_0 is negative in circuit 11. Moreover, the fitted value of R_{tm} is $104670\ \Omega$. Obviously, both values do not have any physical meaning. Consequently, circuit 11 was discarded.

Second, as stated in section 3.2.14, the second Warburg element of circuit 12 is related to water transport phenomena. The fitted value of the time constant of the aforementioned Warburg element is $0.1046\ \mathrm{s}$, as it can be seen in table 5. The characteristic time of water transport phenomena in PEMFC is in the range $10\ s - 100\ s$ [72]. Therefore, the fitted value of τ_{tm} is inconsistent with its physical meaning. For this reason, circuit 12 was discarded.

Third, the fitted exponent of the mass transport related Warburg element is 0.577 in circuit 10, as it can be seen in table 3; and 0.500 in circuit 9, as it can be seen in table 2. According to the physical explanation of circuits 9 and 10, presented in section 3.2, the mentioned Warburg elements are related to oxygen diffusion. The exponent of a Warburg element related to diffusion is equal to 0.5 [77]. Circuit 9 was preferred over circuit 10, since its α_{tm} value is closer to the theoretical value. For this reason, circuit 10 was discarded in this work.

Finally, in the case of circuit 9 no inconsistencies between the fitted values and their physical interpretation were identified. In the case of parameter α_{tm}, its fitted value is 0.5; which is consistent with its physical interpretation (oxygen diffusion). Two different options arise at this point: the transport limitation could be due to diffusional problems of oxygen in the cathodic GDL or in the cathodic CL. In order to select one of the two options, the time constant of the Warburg element can be used. The time constant of a finite length diffusion Warburg element is given by the following expression:

$$\tau_{tm} = \frac{\delta_{dif}^2}{D} \qquad (7)$$

Where δ_{dif} denotes the diffusion layer thickness; and D represents the effective diffusion coefficient. As it can be seen in table 2, the fitted value of τ_{tm} is $0.0903\ s$. The main difference between oxygen diffusion in the GDL and oxygen diffusion in the CL, is the diffusion media. On the one hand, GDLs are porous media [1]; and therefore the oxygen diffusion in the GDL corresponds with the diffusion of a gas in a porous media. Consequently, the effective diffusion coefficient can be determined using the diffusion coefficient in gas phase, and the porosity and tortuosity of the GDL. The corresponding expressions were presented in a previous work [20]. The effective oxygen diffusion coefficient in the GDL, in the operation conditions at which the EIS measurements were performed, was obtained using the mentioned expressions: $D_{GDL} = 0.05\ cm^2 \cdot s^{-1}$. On the other hand, oxygen diffusion in the CL can be considered as the diffusion of oxygen in Nafion® [1]. The diffusion coefficient of oxygen in Nafion® at $30℃$ (the operation temperature at which the EIS measurements were performed) is $D_{CL} = 0.6 \cdot 10^{-6}\ cm^2 \cdot$

s^{-1} [87]. Using these values and expression (7), the diffusion layer thickness can be determined for each one of the assumptions:

$$\delta_{GDL} = \sqrt{\tau_{tm} \cdot D_{GDL}} \approx 672\ \mu m \quad (8)$$

$$\delta_{CL} = \sqrt{\tau_{tm} \cdot D_{CL}} \approx 2.3\ \mu m \quad (9)$$

Consequently, if the mass transport limitations were due to the oxygen diffusion in the GDL, the diffusion layer would have a thickness of around $672\ \mu m$, which is clearly higher than the total thickness of the GDL, that according to the PEMFC supplier is $500\ \mu m$. For this reason, in this case the assumption of mass transport limitations in the GDL was discarded. In the case of oxygen mass transport limitations in the CL, the diffusion layer would have a thickness of around $2.3\ \mu m$, which is consistent with the total thickness of the CL, $10\ \mu m$. Therefore, it was deduced that in this case the mass transport limitations were due to oxygen diffusion in the cathodic CL.

As it can be seen in table 2, α_{dl} is equal to 1. Therefore, in this case the CPE reduces to a pure capacitor. As it was introduced in section 3.2.11, this capacitor is related to the double layer. The double layer capacitance, C_{dl}, is related to the double layer thickness, δ_{dl} [88]:

$$C_{dl} = \frac{\varepsilon \cdot \varepsilon_0 \cdot \gamma \cdot A}{\delta_{dl}} \quad (10)$$

Where ε stands for the dielectric constant and $\varepsilon_0 = 8.8542 \times 10^{-14}\ F \cdot cm^{-1}$ denotes the vacuum permittivity. A represents the geometrical area; and γ is the rugosity factor that relates the geometrical area to the effective catalyst surface. According to the supplier of the commercial PEMFC, $A = 58\ cm^2$ and $\gamma = 300$. The CL can be considered as catalyst particles embedded in a Nafion® layer [1]. The dielectric constant of Nafion® in the operation conditions at which the EIS measurements were performed is around 50 [89]. As it can be seen in table 2, Q_{dl} , which is equal to C_{dl} since $\alpha_{dl} = 1$, is equal to $1.0448\ F$. Using this value in expression (10), the double layer thickness can be estimated:

$$\delta_{dl} = \frac{\varepsilon \cdot \varepsilon_0 \cdot \gamma \cdot A}{C_{dl}} \approx 7.37\ \text{Å} \qquad (11)$$

Similar systems (i.e. solid electrolyte systems) have double layer thicknesses in the range from 3 Å to 10 Å [90]. Therefore, the value of δ_{dl} estimated using circuit 9 is consistent with the bibliographic data of double layer thicknesses for similar systems.

3.3.3. Selected circuit

Since no physical inconsistencies were identified in table 2, a modified version of circuit 9 was selected in this work. The selected circuit is shown in figure 6. In the modified version, the double layer is modelled with a pure capacitance rather than with a CPE; and the Warburg element related to oxygen diffusion in the CL corresponds with a finite length Warburg element ($\alpha_{tm} = 0.5$). The selected circuit does not include any element

associated with the anodic reaction. This is consistent with the well-known fact that the anodic impedance is negligible in PEMFCs.

The selected circuit was fitted to the other two experimental spectra (1A and 4A). Figure 7 shows the fitting of the selected circuit to the 3 experimental EIS spectra in the Nyquist plot; while figure 8 shows the related component diagrams. It can be observed that the selected circuit is able to perfectly reproduce all the experimental EIS spectra. This is consistent with the values of the determination coefficient, which are equal to 99.984% (1A case), 99.983% (4A case) and 99.993% (8A case). Moreover, table 6 gives the values of the parameters of the selected circuit fitted to the 3 experimental EIS spectra. It can be observed that no physically inconsistent parameter values were obtained in the 1A and the 4A spectra fitting.

For the sake of simplicity, this work presents only the results obtained for one set of operation conditions (i.e. an operation temperature of $30℃$; and the same humidification temperature for both gases, $30℃$). However, the selected circuit was fitted to experimental EIS spectra obtained in a wide range of operation conditions. Very good fits were obtained in every case. Moreover, no physically inconsistent parameter values were obtained in any case. The trends with the operation conditions observed for the different parameters are consistent with their physical meaning. For instance, in operation conditions in which flooding is important, the parameters related to oxygen transport (R_{tm} and τ_{tm}) take significantly larger values. This is due to the fact that oxygen transport is heavily hindered in a flooded cell, since the liquid water layer increases the oxygen transport resistance. This explains the well-known expansion of

the low frequency capacitive semicircle [65]. Another example: in operation conditions in which drying is important, parameter R_{int} raises significantly. This is consistent with R_{int}'s physical meaning: the ionic resistance of the PEM membrane increases strongly when the membrane operates in dry conditions. This is the reason for the well-known translation toward higher values of the high frequency intercept with the real axis [91].

4. Conclusions

In this work, an electric equivalent circuit was obtained in order to model the EIS response of an individual cell of a commercial 300W PEMFC stack. The selected circuit is composed by a series connection between a resistance, an inductance, a generalized Warburg element and a C(R(R+L)+W) subcircuit. The advantage of the selected circuit is that besides fitting perfectly the experimental spectra, all its elements have a clear mechanistic meaning: Resistance R_{int} includes all the ohmic losses of the cell, mainly the protonic resistance of the PEM membrane. Inductance L_{cables} is associated to the measurement system cabling. The generalized finite length Warburg element represents the distributed resistance within the cathodic CL. C_{dl} models the double layer; while the R(R+L) subcircuit is related to the ORR kinetics. This subcircuit is responsible for the presence of an inductive loop at low frequencies due to the adsorption and desorption of ORR intermediates. Finally, the finite length diffusion Warburg element is associated to oxygen diffusion in the cathodic CL. The proposed equivalent circuit can be used in order to estimate different physical properties of the studies system (i.e. double layer thickness).

5. Nomenclature

Latin letters

A	Geometrical area (m^2)
C	Capacitance (F)
D	Diffusion coefficient $(m^2 \cdot s^{-1})$
f	Frequency (Hz)
H	Inductance (H)
j	Imaginary unit
N_{par}	Number of model parameters
Q	Constant phase element pseudo-capacitance $(F \cdot s^{\alpha-1})$
R	Resistance (Ω)
R^2	Determination coefficient $(\%)$
s_i	Relative error of the i-th fitted parameter $(\%)$
s_{mean}	Mean error of the fitted parameters $(\%)$
Z	Complex impedance (Ω)
Z'	Real part of complex impedance (Ω)
Z''	Imaginary part of complex impedance (Ω)

Greek letters

α_{CPE}	Constant phase element exponent
α_{tm}	Generalized Warburg element exponent

δ_{dif}	Diffusion layer thickness (m)
δ_{dl}	Double layer thickness (m)
ε	Dielectric constant
ε_0	Permitivity of the vaccum $(F \cdot cm^{-1})$
γ	Rugosity factor
σ_i	Uncertainty related to the i-th fitted parameter
τ_{tm}	Generalized Warburg element time constant (s)
ω	Angular frequency $(rad \cdot s^{-1})$

6. Acknowledgments

The authors are very grateful to the Generalitat Valenciana for its economic support in form of Vali+d grant (Ref: ACIF-2013-268).

7. Bibliography

[1] F. Barbir, PEM fuel cells: theory and practice, Academic Press, London, 2013.

[2] L. Mao, L. Jackson, T. Jackson, J. Power Sources 362 (2017) 39-49.

[3] W. Vielstich, H. Yokokawa and H.A. Gasteiger, Handbook of fuel cells: fundamentals technology and applications, John Wiley & Sons, New York, 2009.

[4] J.J. Giner-Sanz, E.M. Ortega and V. Pérez-Herranz, Int. J. Hydrogen Energ. 39 (2014) 13206-13216.

[5] S. Herden, F. Riewald, J.A. Hirschfeld, M. Perchthaler, J. Power Sources 355 (2017) 36-43.

[6] T. Søndergaard, L.N. Cleemann, H. Becker, D. Aili, T. Steenberg, H.A. Hjuler, L. Seerup, Q. Li, J.O. Jensen, J. Power Sources 342 (2017) 570-578.

[7] S. Herden, J.A. Hirschfeld, C. Lohri, M. Perchthaler, S. Haase, J. Power Sources 364 (2017) 449-457.

[8] M. Tanaka, Y. Takeda, T. Wakiya, Y. Wakamoto, K. Harigaya, T. Ito, T. Tarao, H. Kawakami, J. Power Sources 342 (2017) 125-134.

[9] V. Atanasov, A. Oleynikov, J. Xia, S. Lyonnard, J. Kerres, J. Power Sources 343 (2017) 364-372.

[10] G.R. Molaeimanesh, M. Nazemian, J. Power Sources 359 (2017) 494-506.

[11] S. Chevalier, N. Lavielle, B.D. Hatton, A. Bazylak, J. Power Sources 352 (2017) 272-280.

[12] S. Chevalier, N. Lavielle, B.D. Hatton, A. Bazylak, J. Power Sources 352 (2017) 281-290.

[13] Y. Utaka, R. Koresawa, J. Power Sources 363 (2017) 227-233.

[14] S. Sakaida, Y. Tabe, T. Chikahisa, J. Power Sources 361 (2017) 133-143.

[15] A. Bharti, G. Cheruvally, J. Power Sources 360 (2017) 196-205.

[16] A. Bharti, G. Cheruvally, J. Power Sources 363 (2017) 413-421.

[17] J.K. Dombrovskis, A.E.C. Palmqvist, J. Power Sources 357 (2017) 87-96.

[18] D.E. Glass, G.A. Olah, G.K.S. Prakash, J. Power Sources 352 (2017) 165-173.

[19] Y. Wang, L. Yue, S. Wang, J. Power Sources 344 (2017) 32-38.

[20] J.J. Giner-Sanz, E.M. Ortega and V. Pérez-Herranz, Fuel Cells 15 (2015) 479- 493.

[21] M.A. Danzer and E.P. Hofer, J. Power Sources 190 (2009) 25-33.

[22] J.J. Giner-Sanz, E.M. Ortega and V. Pérez-Herranz, Int. J. Hydrogen Energ. 40 (2015) 11279-11293.

[23] J.J. Giner-Sanz, E.M. Ortega and V. Pérez-Herranz, Fuel Cells 17 (2017) 391-401.

[24] M.A. Danzer and E.P. Hofer, J. Power Sources 183 (2008) 55-61.

[25] J.J. Giner-Sanz, E.M. Ortega and V. Pérez-Herranz, Electrochim. Acta 211 (2016) 1076-1091.

[26] J.J. Giner-Sanz, E.M. Ortega and V. Pérez-Herranz, Electrochim. Acta 209 (2016) 254-268.

[27] J.J. Giner-Sanz, E.M. Ortega and V. Pérez-Herranz, Electrochim. Acta 186 (2015) 598-612.

[28] J.J. Giner-Sanz, E.M. Ortega and V. Pérez-Herranz, J. Electrochem. Soc. 164 (2017) H918-H924.

[29] M.E. Orazem and B. Tribollet, Electrochemical Impedance Spectroscopy, John Wiley & Sons, New Jersey, 2008.

[30] E. Barsoukov and J.R. Macdonald, Impedance Spectroscopy. Theory, experiment and applications, John Wiley & Sons, New Jersey, 2005.

[31] A. Lasia, Electrochemical Impedance Spectrscopy and its applications, Springer, London, 2014.

[32] D.D. Macdonald, Electrochim. Acta 51 (2006) 1376-1388.

[33] M. Ciureanu, R. Roberge, J. Phys. Chem. 105 (2001) 3531-3539.

[34] N.J. Wagner, J. Appl. Electrochem. 32 (2002) 859-863.

[35] N. Wagner, E. Gulzow, J. Power Sources 127 (2004) 341-347.

[36] P.M. Gomadam, J.W. Weidner, Int. J. Energ. Res. 29 (2005) 1133-1151.

[37] X. Yuan et al., J. Power Sources 161 (2006) 920-928.

[38] W. Merida, D.A. Harrington, J.M. Le Canut, G. Mclean, J. Power Sources 161 (2006) 264-274.

[39] J.M. Le Canut, R.M. Abouatallah, D.A. Harrington, J. Electrochem. Soc. 153 (2006) A857-864.

[40] N. Fouquet, C. Doulet, C. Nouillant, G. Dauphin-Tanguy, B. Ould-Bouamama, J. Power Sources 159 (2006) 905-913.

[41] W.H. Zhu, R.U. Payne, B.J. Tatarchuk, J. Power Sources 168 (2007) 211-217.

[42] A.M. Dhirde, N.V. Dale, H. Salehfar, M.D. Mann, T.H. Han, IEEE T. Energy Conver. 25 (2010) 778-786.

[43] S. Roda, S. Sailler, F. Druart, P.X. Thivel, Y. Bultel, P. Ozil, J. Appl. Electrochem. 40 (2010) 911-920.

[44] J.H. Lee, J.H. Lee, W. Choi, K.W. Park, H.Y. Sun, J.H. Oh, J. Power Sources 195 (2010) 6001-6007.

[45] I. Pivac, B. Simic, F. Barbir, J. Power Sources 365 (2017) 240-248.

[46] B.P. Setzler, T.F. Fuller, J. Electrochem. Soc. 162 (2015) F519-F530.

[47] R. de Levie, Adv. Electroch. El. Eng. 6 (1967) 329-397.

[48] A. Lasia, J. Electroanal. Chem. 397 (1995) 27-33.

[49] A. Lasia, J. Electroanal. Chem. 428 (1997) 155-164.

[50] T.E. Springer, T.A. Zawodzinski, M.S. Wilson, S. Gottesfeld, J. Electrochem. Soc. 142 (1996) 587-599.

[51] Q.Z. Guo, R.E. White, J. Electrochem. Soc. 151 (2004) E133-E149.

[52] A.A. Kulikovski, J. Electroanal. Chem. 669 (2012) 28-34.

[53] A.A. Kulikovski, Electrochimica Acta 147 (2014) 773-777.

[54] A.A. Kulikovski, Electrochimica Acta 196 (2016) 231-235.

[55] A.A. Kulikovski, Electrochimica Acta 225 (2017) 559-565.

[56] I.A. Schneider, M.H. Bayer, A. Wokaun, G.G. Scherer, J. Electrochem. Soc. 155 (2008) B783-B792.

[57] S.M.R. Niya, M. Hoorfar, Electrochimica Acta 120 (2014) 193-203.

[58] K. Wiezell, N. Holmstrom, G. Lindbergh, J. Electrochem. Soc. 159 (2012) F379-F392.

[59] N. Holmstrom, K. Wiezell, G. Lindbergh, J. Electrochem. Soc. 159 (2012) F369-F378.

[60] B.P. Setzler, T.F. Fuller, ECS Transactions 58 (2013) 95-107.

[61] O. Antoine, Y. Bultel, R. Durand, J. Electroanal. Chem. 499 (2001) 85-94.

[62] S.K. Roy, M.E. Orazem, B. Tribollet, J. Electrochem. Soc. 154 (2007) B1378-B1388.

[63] Y. Bultel, L. Genies, O. Antoine, P. Ozil, R. Durand, J. Electroanal. Chem. 527 (2002) 143-155.

[64] M. Mathias, D. Baker, J. Zhang, Y. Liu, W. Gu, ECS Transactions 13 (2008) 129-152.

[65] A.Z. Weber, R.L. Borup, R.M. Darling, P.K. Das, T.J. Dursch, W. Gu, D. Harvey, A. Kusoglu, S. Litster, M.M. Mench, R. Mukundan, J.P. Owejan, J.C. Pharoah, M. Secanell, I.V. Zenyuk, J. Electrochem. Soc. 161 (2014) F1254-F1299.

[66] S.M.R. Niya, M. Hoorfar, J. Power Sources 240 (2013) 281-293.

[67] J.J. Giner-Sanz, E.M. Ortega and V. Pérez-Herranz, Fuel Cells 16 (2016) 469-479.

[68] J.J. Giner-Sanz, E.M. Ortega and V. Pérez-Herranz, Electrochim. Acta 174 (2015) 1290-1298.

[69] M. Chandesris et al., Electrochim. Acta 180 (2015) 581-590.

[70] A. Battistel et al., Electrochim. Acta 135 (2014) 133-138.

[71] T.J.P. Freire and E.R. Gonzalez, J. Electroanal. Chem. 503 (2001) 57- 68.

[72] V.A. Paganin et al., Electrochim. Acta 43 (1998) 3761-3766.

[73] M. Eikerling and A.A. Kornyshev, J. Electroanal. Chem. 453 (1998) 89-106.

[74] M. Eikerling and A.A. Kornyshev, J. Electroanal. Chem. 475 (1999) 107-123.

[75] S.K. Roy, Use of Impedance Spectroscopy to Investigate Factors that Influence the Performance and Durability of PEM Fuel Cells. PhD Tesis, University of Florida, 2008.

[76] J.T. Müller, P.M. Urban and W.F. Hölderich, J. Power Sources 84 (1999) 157-160.

[77] J.P Diard, B. Le Gorrec and C. Montella, Handbook of Electrochemical Impedance Spectroscopy, Bio-logic, Paris, 2009.

[78] X.Z. Yuan et al., Electrochemical impedance spectroscopy in PEM fuel cells. Fundamentals and applications, Springer, London, 2010.

[79] J.H. Sluyters, Recl. Trav. Chim. Pay. B. 79 (1960) 1092-1100.

[80] K. Nisancioglu and J. Newman, J. Electrochem. Soc. 159 (2012) E59-E61.

[81] S.L. Wu et al., Electrochimica Acta 131 (2014) 3-12.

[82] D.A. Harrington and B.E. Conway, Electrochim. Acta 32 (1987) 1703-1712.

[83] J. Zhang, PEM fuel cell electrocatalysts and catalyst layers: fundamentals and applications, Springer Science & Business Media, New York, 2008.

[84] M.E. Orazem and B. Tribollet, Electrochim. Acta 53 (2008) 7360-7366.

[85] O. Antoine et al., Electrochim. Acta 43 (1998) 3681-3691.

[86] I. Sadli, Modelisation par Impedance d'une Pile à Combustible PEM pour Utilisation en Electronique de Puissance, PhD Tesis, L'Institut National Polytechnique de Lorraine, 2006.

[87] V.A. Sethuraman et al., Electrochim. Acta 54 (2009) 6850-6860.

[88] B. Hirschorn et al., Electrochim. Acta 55 (2010) 6218-6227.

[89] S.J. Paddison et al., J. New Mat. Elect. Syst. 3 (2000) 293-300.

[90] F. Scholz, Electroanalytical Methods. Guide to Experiments and Applications, Springer, London, 2010.

[91] J.J. Giner-Sanz, E.M. Ortega and V. Pérez-Herranz, J. Power Sources (2018).

Table 1. EIS measurement parameters

Measurement parameter	Value
Integration time	$1.0\ s$
Number of integration cycles	$5\ cycles$
Number of stabilization cycles	$15\ cycles$
Maximum stabilization time	$1.0\ s$
Minimum stabilization cycle fraction	0.00

Table 2. Circuit 9 fitted parameters

$Parameter$	$Fitted\ value$	$Error\ (\%)$
$R_{int}\ (\Omega)$	0.005685	0.62
$L_{cables}\ (\mathrm{H})$	5.18×10^{-8}	1.29
$R_{dr}\ (\Omega)$	0.01284	4.08
$\tau_{dr}\ (\mathrm{s})$	0.01051	5.58
α_{dr}	0.452	2.86
$Q_{dl}\ (F \cdot s^{\alpha_{dl}-1})$	1.0448	16.31
α_{dl}	1.000	0.42
$R_{tm}\ (\Omega)$	0.003618	7.21
$\tau_{tm}\ (\mathrm{s})$	0.0903	3.72
α_{tm}	0.500	2.91
$R_{\infty}\ (\Omega)$	0.007258	6.54
$L\ (\mathrm{H})$	0.2667	15.44
$R_0\ (\Omega)$	0.02483	16.60

Table 3. Circuit 10 fitted parameters

$Parameter$	$Fitted\ value$	$Error\ (\%)$
$R_{int}\ (\Omega)$	0.005786	0.98
$L_{cables}\ (\mathrm{H})$	5.00×10^{-8}	2.03
$R_{dr}\ (\Omega)$	0.01559	1.76
$\tau_{dr}\ (\mathrm{s})$	0.01703	8.92
α_{dr}	0.463	3.10
$Q_{dl}\ (F \cdot s^{\alpha_{dl}-1})$	0.7978	7.45
α_{dl}	1.000	0.54
$R_{tm}\ (\Omega)$	0.003951	15.59
$\tau_{tm}\ (\mathrm{s})$	0.0935	4.96
α_{tm}	0.577	4.08
$R_{\infty}\ (\Omega)$	0.003933	19.25
$L\ (\mathrm{H})$	0.4331	9.29
$R_0\ (\Omega)$	0.01561	8.53

Table 4. Circuit 11 fitted parameters

$Parameter$	$Fitted\ value$	$Error\ (\%)$
$R_{int}\ (\Omega)$	0.005538	0.75
$L_{cables}\ (\mathrm{H})$	5.16×10^{-8}	1.86
$R_{dr}\ (\Omega)$	0.01673	1.06
$\tau_{dr}\ (\mathrm{s})$	0.04613	3.25
α_{dr}	0.380	1.36
$Q_{dl}\ (F \cdot s^{\alpha_{dl}-1})$	0.5368	2.28
α_{dl}	1.000	0.58
$R_{tm}\ (\Omega)$	104670	0.40
$\tau_{tm}\ (\mathrm{s})$	0.0044	6.09
α_{tm}	0.502	0.02
$R_{\infty}\ (\Omega)$	0.007649	2.64
$L\ (\mathrm{H})$	14.4521	6.09
$R_0\ (\Omega)$	-9999.99	0.92

Table 5. Circuit 12 fitted parameters

$Parameter$	$Fitted\ value$	$Error\ (\%)$
$R_{int}\ (\Omega)$	0.005800	1.06
$L_{cables}\ (\mathrm{H})$	4.99×10^{-8}	2.04
$R_{dr}\ (\Omega)$	0.01520	2.19
$\tau_{dr}\ (\mathrm{s})$	0.01794	10.00
α_{dr}	0.465	3.77
$Q_{dl}\ (F \cdot s^{\alpha_{dl}-1})$	0.8886	10.52
α_{dl}	1.000	0.53
$R_{tm}\ (\Omega)$	0.004486	18.28
$\tau_{tm}\ (\mathrm{s})$	0.1046	4.16
α_{tm}	0.574	4.22
$R_{\infty}\ (\Omega)$	0.003768	20.54
$L\ (\mathrm{H})$	0.1002	41.08
$R_0\ (\Omega)$	0.00162	5.58

Table 6. Parameters of the selected circuit fitted to the 3 experimental EIS spectra

$Parameter$	$I_{DC} = 1A$	$I_{DC} = 4A$	$I_{DC} = 8A$
R_{int} (mΩ)	6.350 ± 0.062	5.989 ± 0.041	5.685 ± 0.035
L_{cables} (nH)	52.0 ± 1.1	52.9 ± 1.3	51.17 ± 0.67
R_{dr} (mΩ)	16.73 ± 0.99	14.65 ± 0.74	12.84 ± 0.52
τ_{dr} (s)	13.70 ± 0.94	9.89 ± 0.45	10.51 ± 0.60
α_{dr}	0.451 ± 0.036	0.467 ± 0.012	0.452 ± 0.013
C_{dl} (F)	0.519 ± 0.055	0.922 ± 0.016	1.045 ± 0.027
R_{tm} (mΩ)	0.93 ± 0.46	1.01 ± 0.18	3.62 ± 0.26
τ_{tm} (ms)	51.4 ± 2.3	70.2 ± 5.9	90.3 ± 3.4
R_{∞} (mΩ)	21.95 ± 0.94	9.25 ± 0.72	7.26 ± 0.48
L (H)	0.660 ± 0.078	0.125 ± 0.022	0.267 ± 0.041
R_0 (mΩ)	144 ± 15	32.9 ± 6.0	24.8 ± 4.1

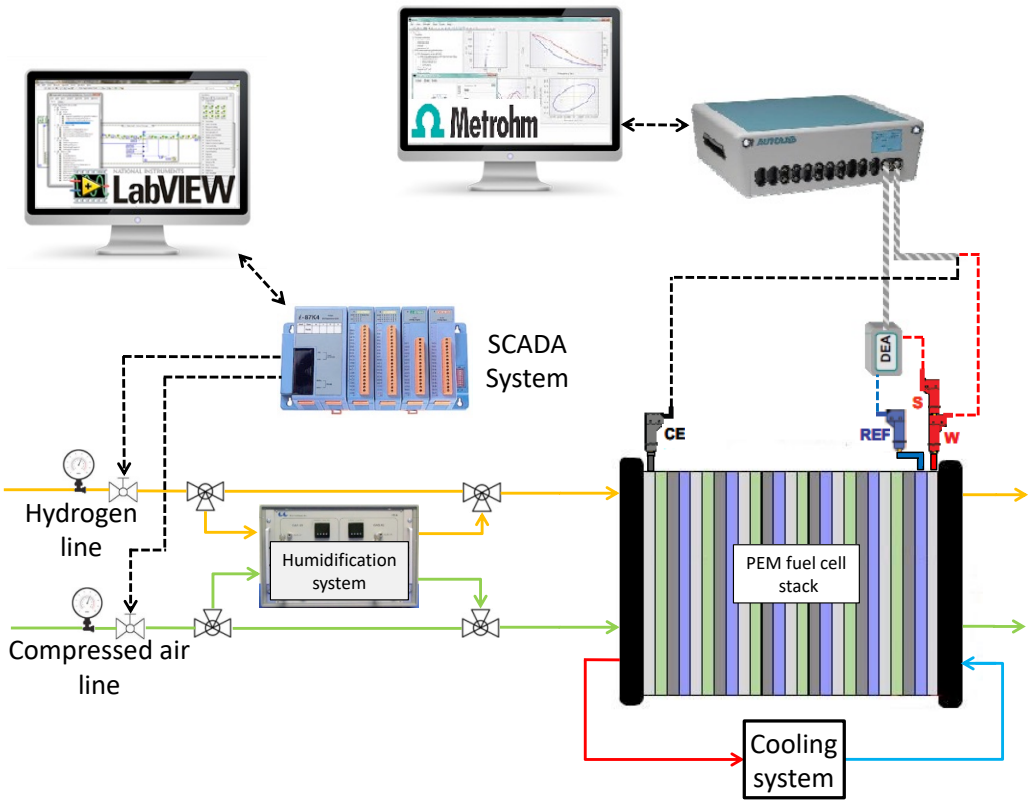

Figure 1. Experimental setup

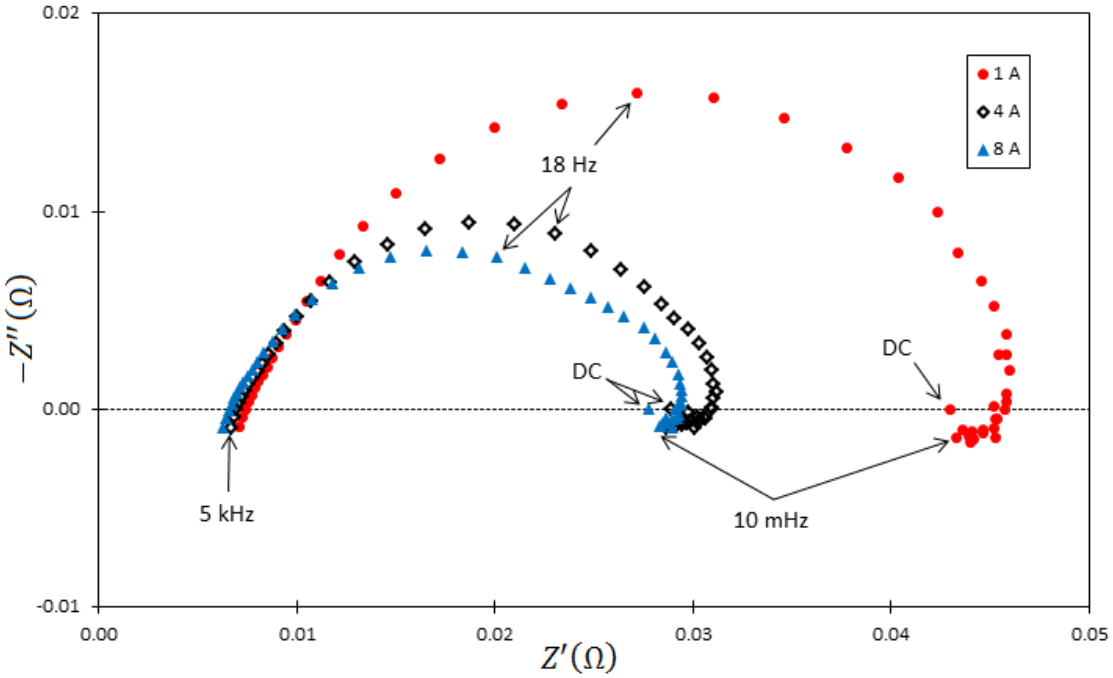

Figure 2. Experimental EIS spectra

(a) Resistance

(b) Inductance

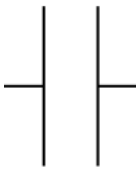

(c) Capacitance

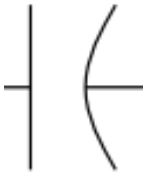

(d) Constant phase element

(e) Generalized finite length Warburg element

Figure 3. Equivalent circuit symbols

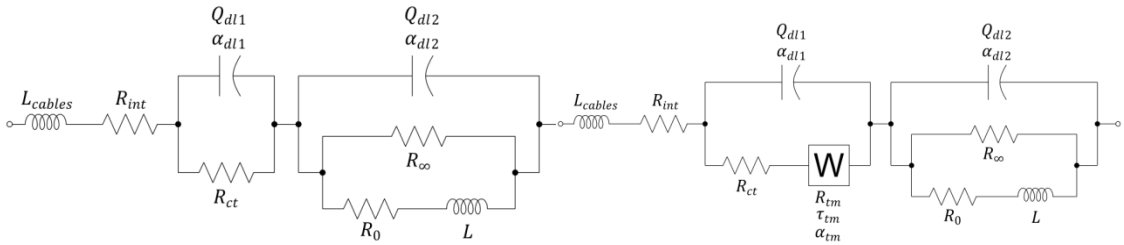

(a) Circuit 1 (b) Circuit 2

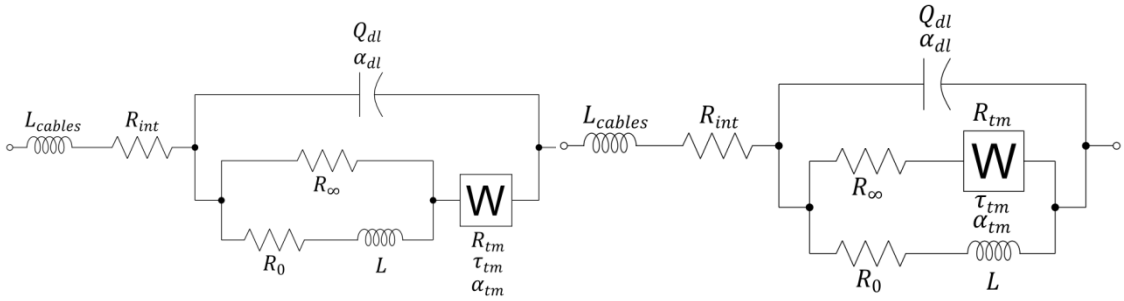

(c) Circuit 3 (d) Circuit 4

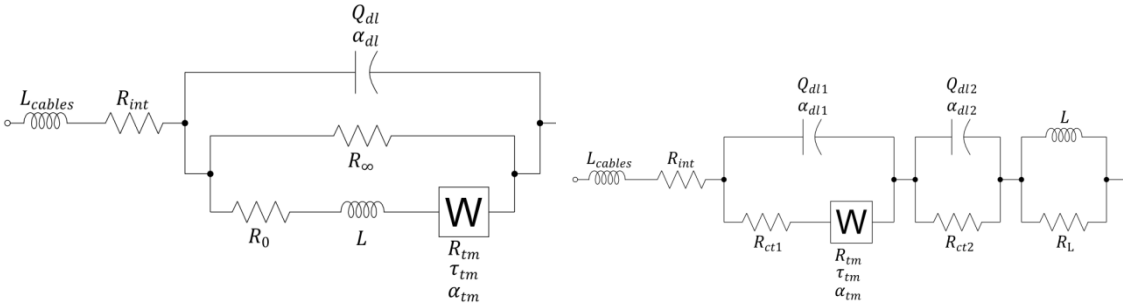

(e) Circuit 5 (f) Circuit 6

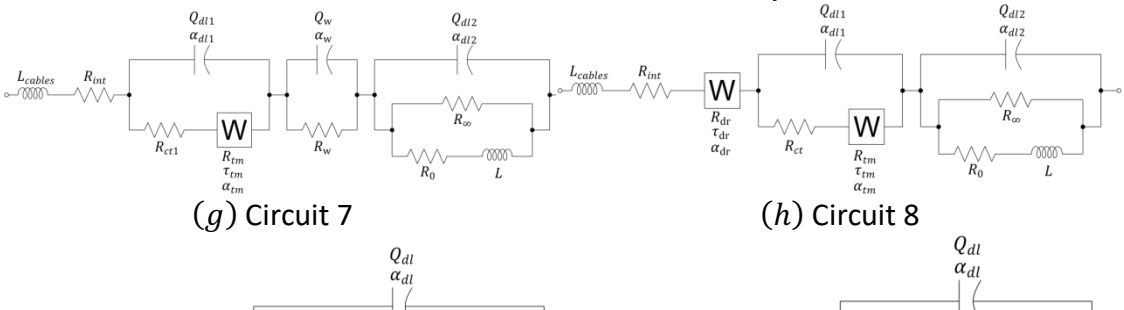

(g) Circuit 7 (h) Circuit 8

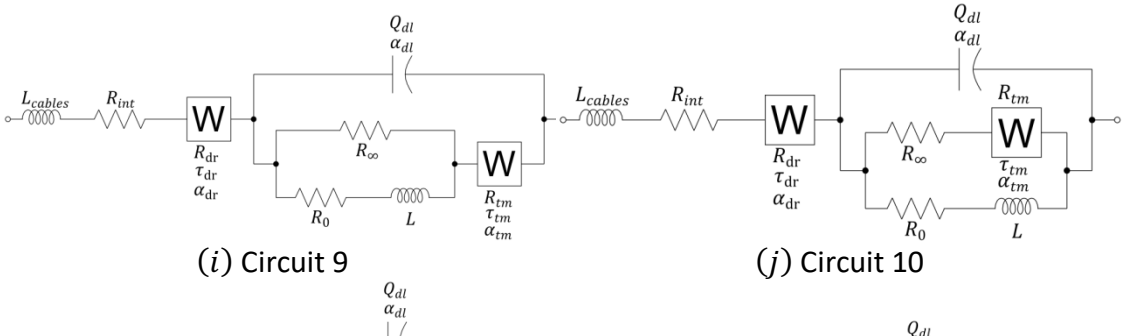

(i) Circuit 9 (j) Circuit 10

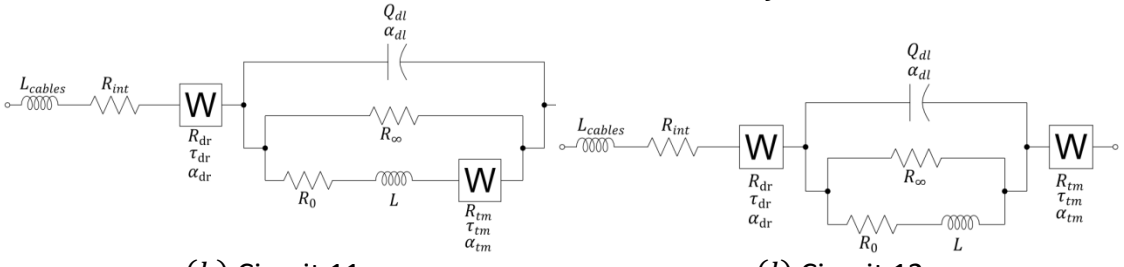

(k) Circuit 11 (l) Circuit 12

Figure 4. Considered electrical equivalent circuits

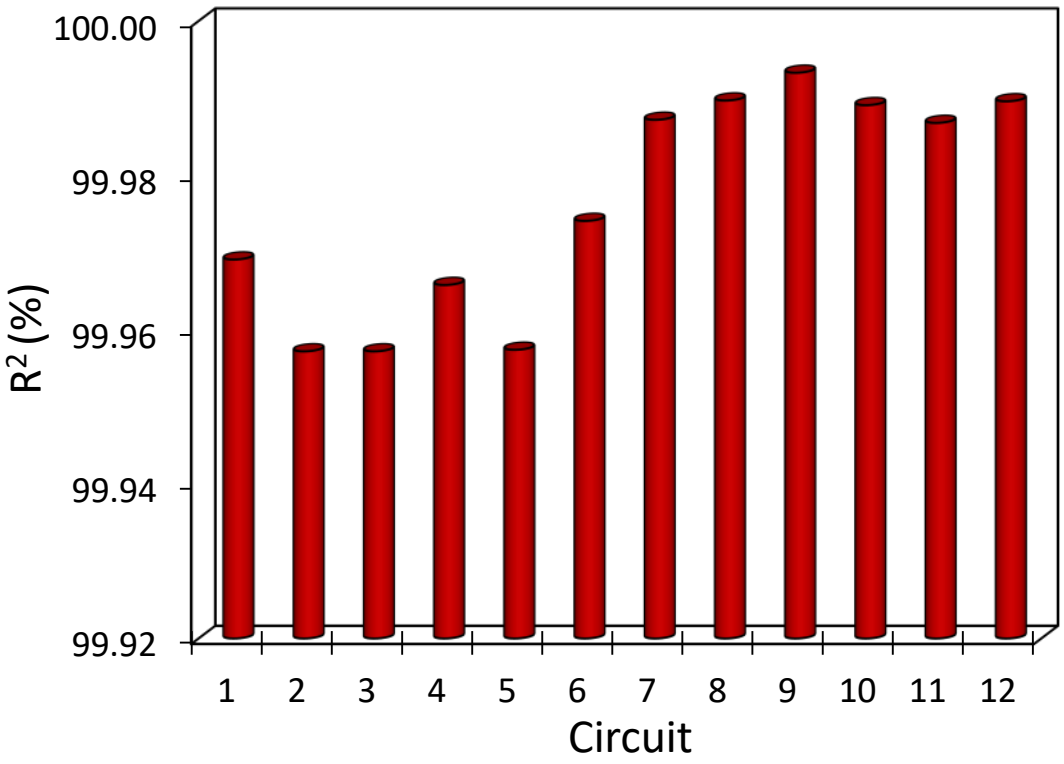

(a) Determination coefficient

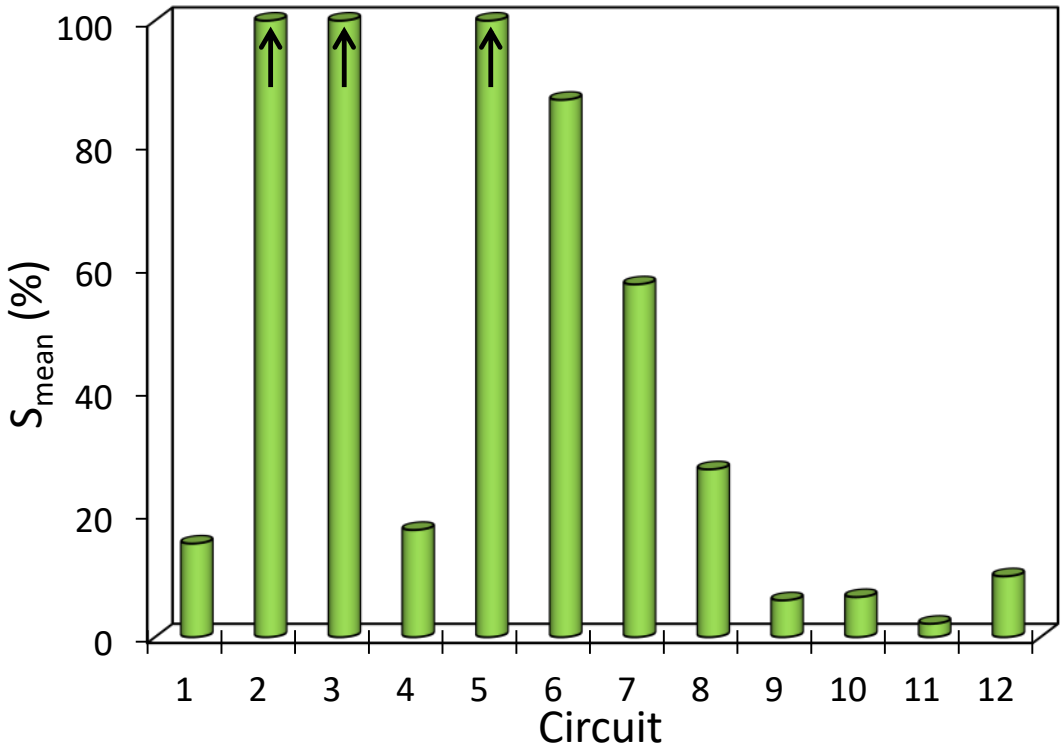

(b) Mean error of the fitted parameters

Figure 5. Determination coefficient and mean error of the parameters, of the fitting of the 8A experimental EIS spectrum to each equivalent circuit

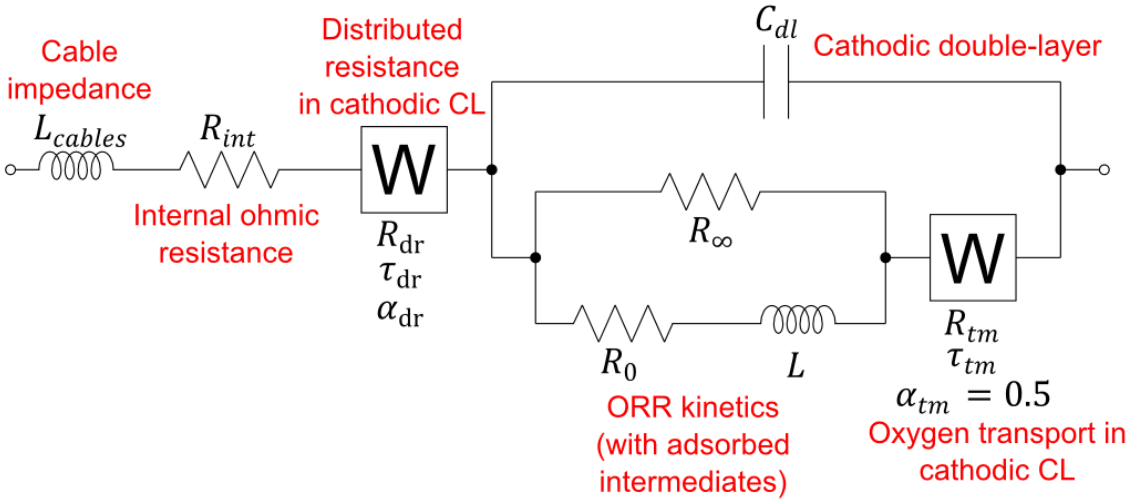

Figure 6. Selected circuit

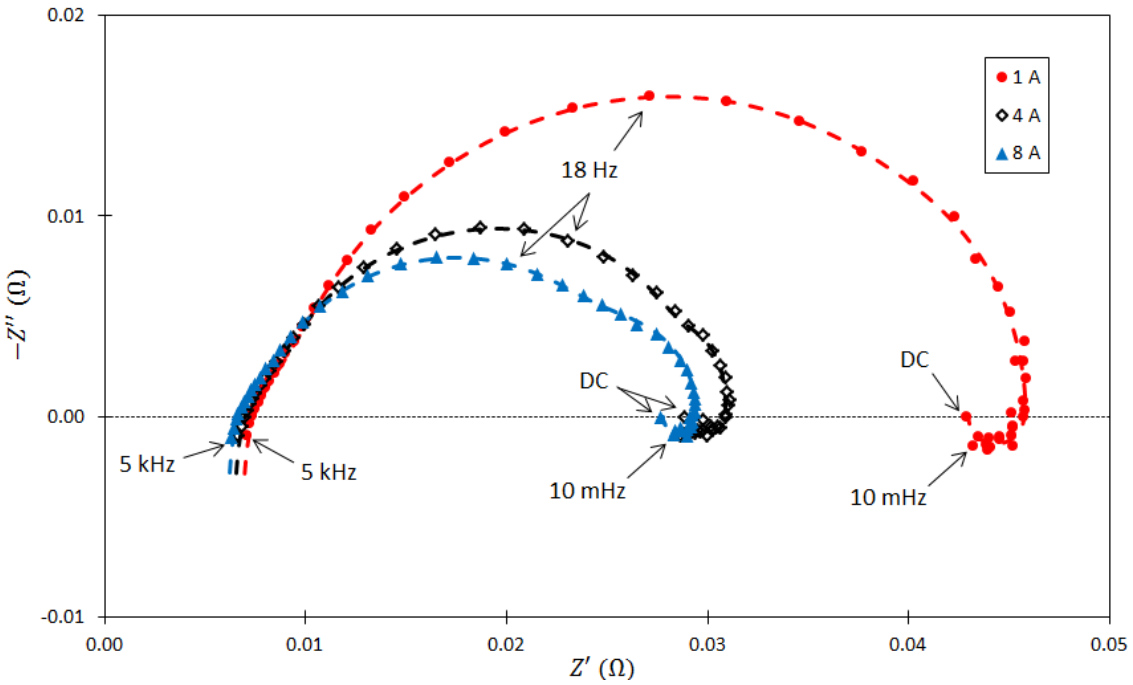

Figure 7. Fitting of the selected circuit (dashed lines) to the different experimental EIS spectra (dots) in the Nyquist plot

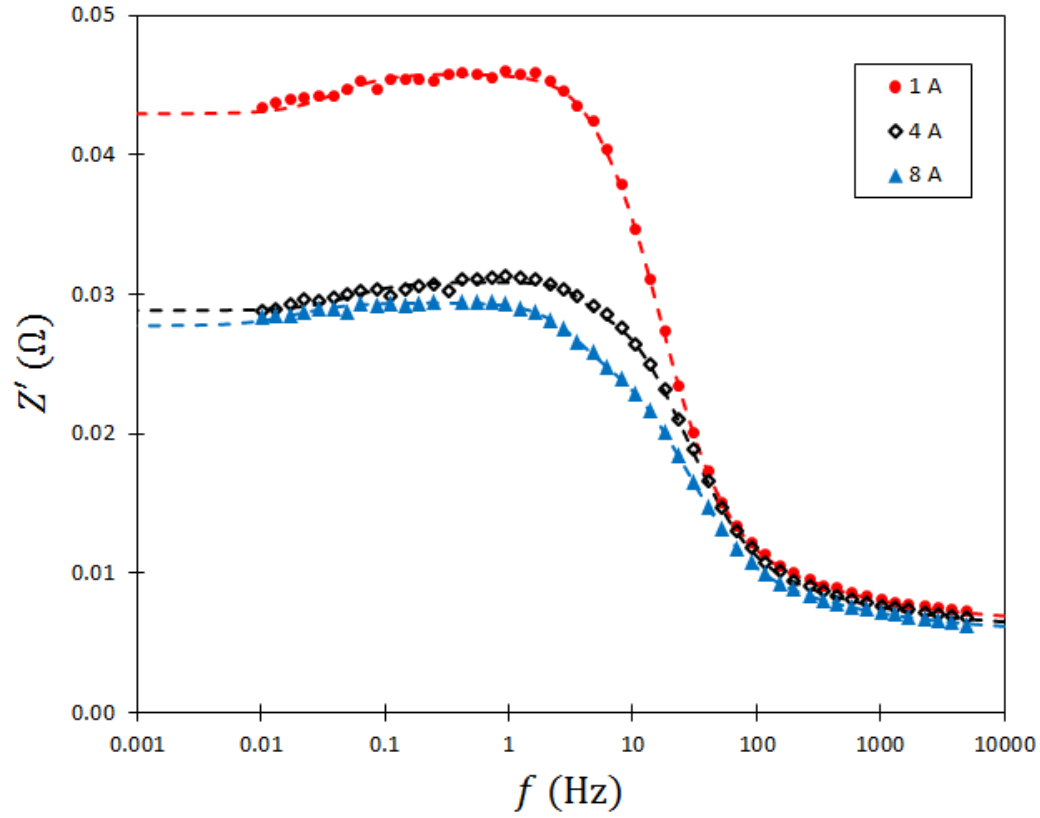

(a) Real part

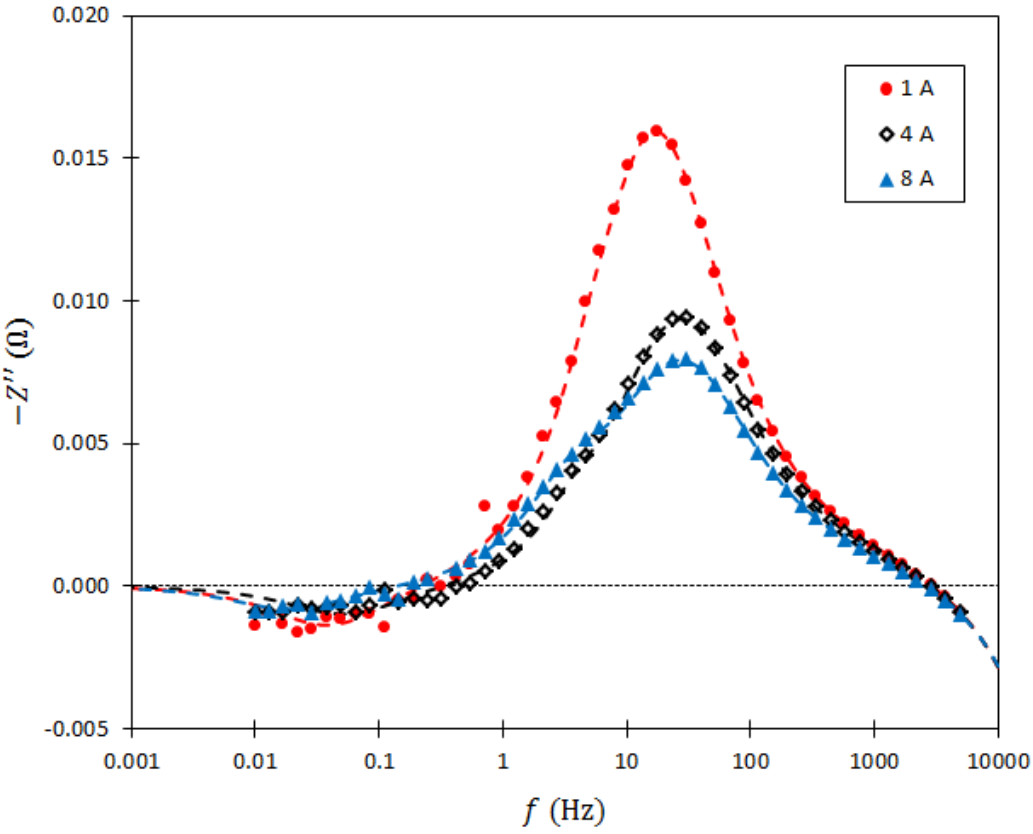

(b) Imaginary part

Figure 8. Fitting of the selected circuit (dashed lines) to the different experimental EIS spectra (dots) in the component plots